

Tough and strong bioinspired high-entropy all-ceramics with a contiguous network structure

Received: 17 January 2025

Accepted: 5 May 2025

Published online: 17 May 2025

 Check for updatesZijie Zhu^{1,3}, Yiwen Liu^{1,3}, Yuanbin Qin^{2,3}, Fangchao Gu¹, Lei Zhuang¹✉, Hulei Yu¹ & Yanhui Chu¹✉

Developing bioinspired all-ceramics with plastic phases is considered one of the most effective ways to simultaneously achieve enhanced strength and toughness in ceramic materials for high-temperature applications. Here we explore tough and strong bioinspired high-entropy all-ceramics with a contiguous network structure that are able to serve up to 1300 °C. Specifically, we develop the high-entropy all-ceramics, featuring a unique contiguous network distribution of the Cr₇C₃ plastic phase within the predominant high-entropy carbide (HEC) hard phase, through a high-entropy composition-engineering strategy. The resulting materials exhibit impressive fracture initiation toughness of $12.5 \pm 1.5 \text{ MPa}\cdot\text{m}^{1/2}$ and flexural strength of $613 \pm 52 \text{ MPa}$ at room temperature, as well as ~97% strength retention up to 1300 °C due to their good high-temperature stability, surpassing the performance of most other reported bioinspired ceramics. Further experimental and theoretical investigations demonstrate that the Cr₇C₃ phase can undergo plastic deformation by forming nanoscale shear bands with significant crystal defects, resulting in multiple toughening mechanisms involving crack-bridging of unfractured Cr₇C₃ ligaments and crack deflection in the HEC/Cr₇C₃ all-ceramics. This work successfully develops tough and strong bioinspired high-entropy all-ceramics capable of serving up to 1300 °C, offering an innovative strategy that facilitates further design of bioinspired ceramics applicable at higher temperatures.

Structural materials play a vital role in a wide range of applications, including advanced manufacturing, metallurgy, chemical industry, aerospace etc¹. Among all characteristics, toughness and strength are two of the most important properties for their practical applications. Unfortunately, these two properties are mutually exclusive, making it challenging to optimize mechanical performance in structural materials^{2,3}. Such strong coupling is particularly pronounced in structural ceramics, which are well known for their good strength due to strong chemical bonds. The strength also enables their use in a wide range of applications in extreme environments, including high

temperature and pressure, and harsh wear conditions^{4–6}. However, these ceramics usually show brittle nature i.e., limited toughness, leading to sudden catastrophic failures during practical service⁷. Therefore, to ensure the service reliability of structural ceramics, it is critical to improve their toughness without sacrificing their high strength.

Through an evolutionary process spanning millions of years, nature has perfected the design and manufacturing of hierarchical multifunctional materials that outperform their synthetic counterparts⁸. Typically, by combining brittle minerals with soft

¹School of Materials Science and Engineering, South China University of Technology, Guangzhou 510641, China. ²State Key Laboratory for Mechanical Behavior of Materials, Xi'an Jiaotong University, Xi'an 710049, China. ³These authors contributed equally: Zijie Zhu, Yiwen Liu, Yuanbin Qin.

✉ e-mail: lzhuang@scut.edu.cn; chuyh@scut.edu.cn

organic molecules to establish brick-and-mortar structure (Fig. 1a), nacre has shown great enhancement in fracture resistance⁹, providing significant inspiration for the ceramic engineering community. Inspired by this unique structure, many bioinspired ceramics with high toughness have hitherto been successfully developed. For example, polymers such as polymethyl methacrylate (PMMA)^{10,11}, polyvinyl alcohol (PVA)¹², and paraffin wax (PW)¹³ have been employed as the soft mortar phase, and the resulting polymer/ceramic hybrid materials demonstrate enhanced fracture initiation toughness (K_{IC}) of 0.7–10.5 MPa·m^{1/2} and flexural strength of 77–220 MPa. Nevertheless, owing to the low melting points of polymer phases, their strength suffers from severe deterioration even at mild temperatures (200 °C or below). These limitations hinder the practical applications of polymer/ceramic hybrid materials, especially at elevated temperatures. To address these issues, researchers have proposed substituting polymers with metals e.g., Al¹⁴ and Ni¹⁵, achieving K_{IC} and flexural strength of 4.9–6.7 MPa·m^{1/2} and 228–294 MPa, respectively. Despite the efforts made, the developed bioinspired metal/ceramic hybrid materials still fail to meet the requirements for potential applications at elevated temperatures, primarily because of the limited softening temperatures of metals that usually fall below 1000 °C.

To solve this problem, a better option would be to develop all-ceramic nacre-like alternatives, yet their improvement in strength is typically limited. The structure of spongy bone, another representative example of natural structural materials from bone tissue, is made of a three-dimensional contiguous network of trabeculae (Fig. 1b). This special network structure facilitates uniform stress distribution in multiple directions, enabling spongy bone to show superior mechanical properties, e.g., ultrahigh specific strength and fracture resistance¹⁶. As a result, by combining the unique structures of nacre and spongy bone, it is expected that one could develop all-ceramic materials with both improved toughness and strength (Fig. 1c). However, two critical challenges still remain: one is that very few ceramics capable of plasticity have been explored (Si₃N₄⁷ and La₂O₃¹⁷ have been shown to have plasticity but they necessitate strict crystallographic

orientations), and the other is the great challenge of achieving uniform contiguous network distribution of plastic ceramics as soft phases within bioinspired all-ceramic materials. In order to enable diverse possibilities in structural design and performance adjustment, a promising high-entropy composition-engineering strategy was proposed in the ceramic community in 2015^{18–25}. For example, nanoplate-toughened high-entropy carbides (HECs)²⁶ and dual-phase high-entropy boride-carbide ceramics²⁷ have been successfully developed by using this strategy, showing significant enhancement in mechanical properties. Therefore, the high-entropy composition-engineering strategy is expected to improve bioinspired all-ceramics with homogeneous distributions of plastic phases.

In this work, we realize the design of bioinspired all-ceramics that feature a contiguous network of the Cr₇C₃ plastic phase uniformly distributed within the predominant HEC [i.e., (Hf, Zr, Ta, Nb, Ti, Cr)C] hard phase, through the high-entropy composition-engineering strategy. Specifically, the resulting HEC/Cr₇C₃ all-ceramics show high K_{IC} of 12.5 ± 1.5 MPa·m^{1/2} and flexural strength of 613 ± 52 MPa at room temperature (RT), and good strength retention of ~97% up to 1300 °C, surpassing the performance of most other reported bioinspired ceramics. Further in-situ experimental and theoretical investigations provide compelling evidence that the Cr₇C₃ phase can plastically deform under load, achieving a ~30.8% compression strain through forming nanoscale shear bands with significant crystal defects. This plastic deformation behavior, which does not rely on specific crystallographic orientations, effectively enriches the toughening mechanisms in HEC/Cr₇C₃ all-ceramics. Our materials are promising in numerous applications e.g., advanced manufacturing, metallurgy, chemical industry, and aerospace, especially at elevated temperatures.

Results and discussion

Fabrication of HEC/Cr₇C₃ all-ceramics

To realize the fabrication of tough and strong high-entropy all-ceramics, two key steps are required: i) the synthesis of core-shell intermediate powders (the HEC core coated with the Cr₇C₃ shell)

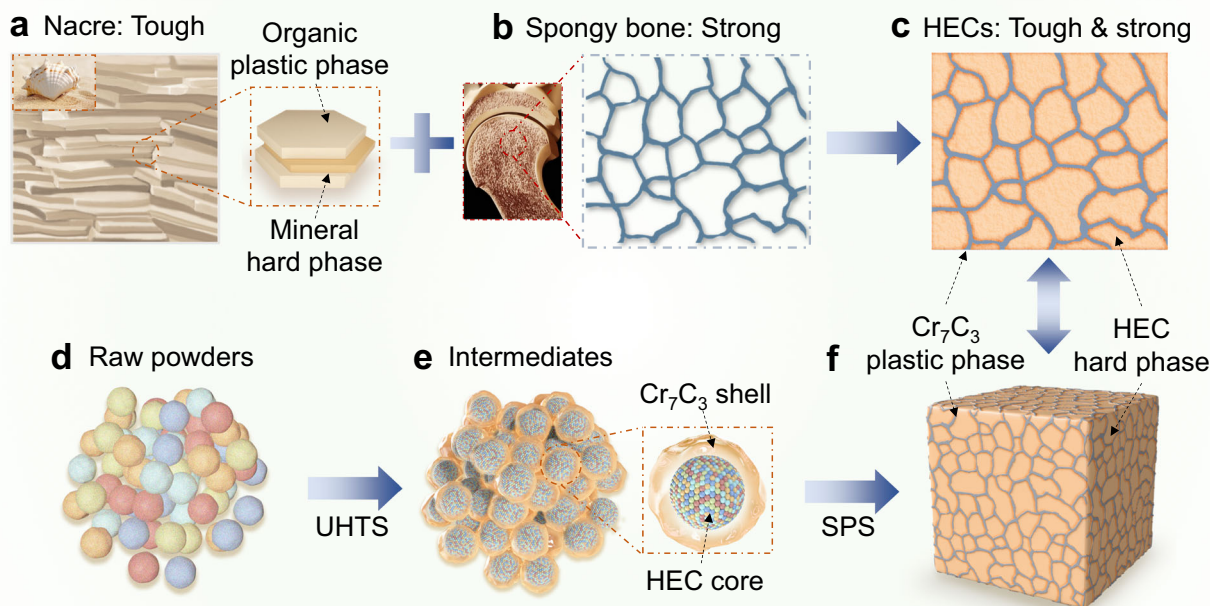


Fig. 1 | Schematic of bioinspired design and fabrication of high-entropy carbide (HEC)/Cr₇C₃ all-ceramics. **a** Brick-and-mortar structure of nacre. **b** Contiguous network structure of spongy bone. **c** Tough and strong all-ceramics with a contiguous network distribution of the Cr₇C₃ plastic phase within the predominant HEC hard phase. Fabrication process of the tough and strong all-ceramics:

d Uniformly mixing the different raw powders (represented as colored spheres) and then heating the mixture to high temperature within seconds using an ultrafast high-temperature synthesis (UHTS) technique, **e** densifying the obtained HEC/Cr₇C₃ core-shell intermediate powders using a spark plasma sintering (SPS) technique, and **f** resulting in the final HEC/Cr₇C₃ all-ceramics.

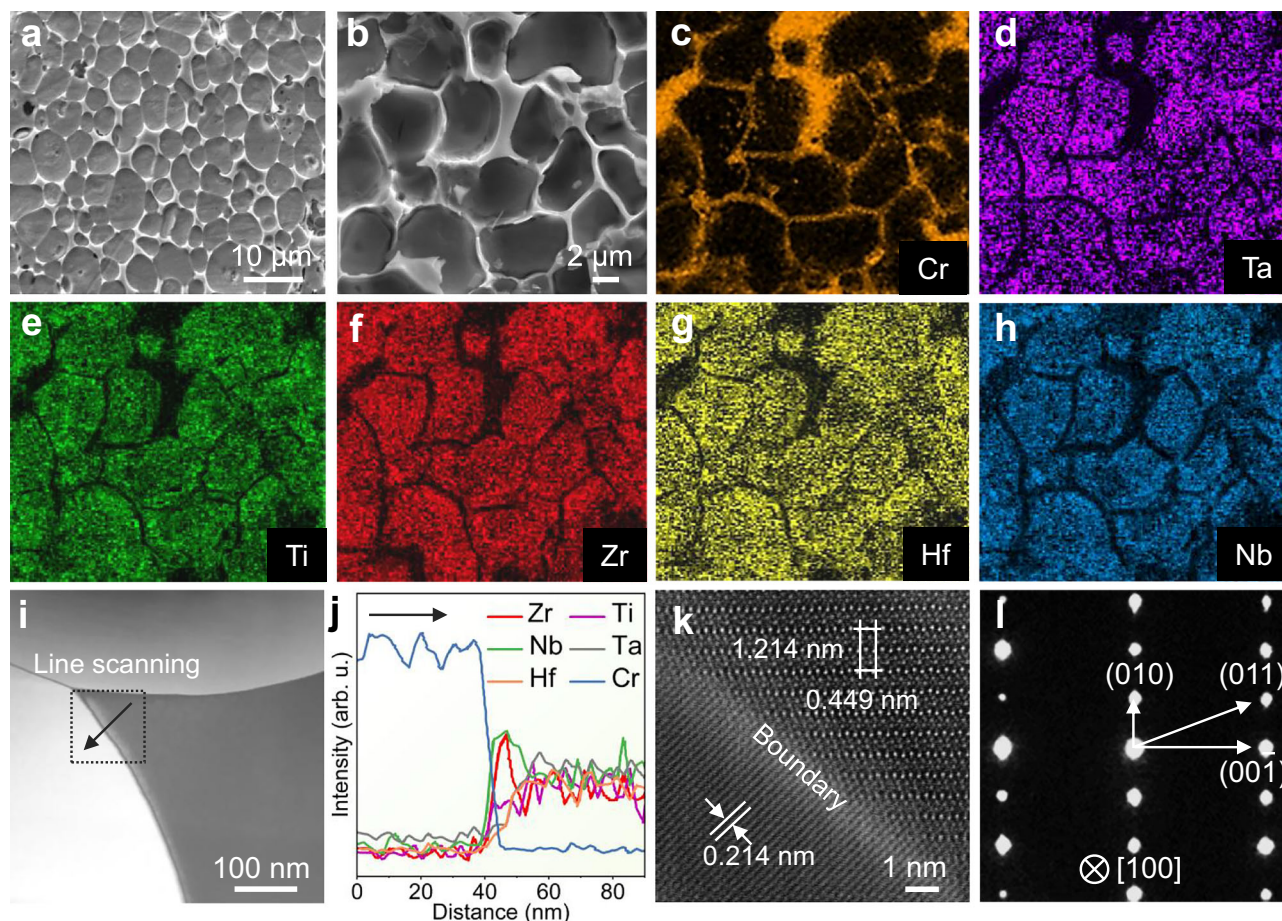


Fig. 2 | Phase composition and microstructure of high-entropy carbide (HEC)/Cr₇C₃ all-ceramics. Low- (a) and high-magnification (b) scanning electron microscope (SEM) images of samples after corrosion in aqua regia. Corresponding energy dispersive spectroscopy (EDS) maps of (b) for different elements: Cr (c), Ta (d), Ti (e), Zr (f), Hf (g), and Nb (h). i Low-magnification high-angle annular dark field (HAADF)-scanning transmission electron microscope (STEM) image of a grain boundary between HEC and Cr₇C₃ phases. j Elemental line scanning results of (i).

The black arrow represents the scanning direction in (i). k High-magnification HAADF-STEM image of Cr₇C₃ and HEC grains with a grain boundary. Specifically, the (010) and (001) planes, with *d*-spacings of 1.214 nm and 0.449 nm, respectively, correspond to orthorhombic Cr₇C₃; while the (100) plane, with a *d*-spacing of 0.214 nm, belongs to face-centered cubic (*fcc*)-HEC. l SAED pattern of the upper grain in (i). Source data are provided as a Source Data file.

through ultrafast high-temperature sintering (UHTS) (Fig. 1d, e); ii) the densification of as-synthesized HEC/Cr₇C₃ core-shell intermediate powders to achieve a contiguous network distribution of Cr₇C₃ within predominant HEC via spark plasma sintering (SPS) (Fig. 1f). Specifically, to synthesize HEC/Cr₇C₃ core-shell intermediate powders, we first calculated Gibbs free energy of these two reaction products. As shown in Supplementary Fig. 1, raw Cr₂O₃ powders are thermodynamically more favorable to react with carbon to form the Cr₇C₃ phase than to participate in solid-solution reactions to form HECs. The scanning electron microscope (SEM) image and energy dispersive spectroscopy (EDS) maps in Supplementary Fig. 2a demonstrate notable differences in elemental distributions between Cr and the other elements in the as-synthesized intermediate powders. The scanning transmission electron microscope (STEM) image along with EDS results confirm that Cr atoms accumulate on the exterior of grains, resulting in the formation of a core-shell microstructure (see Supplementary Fig. 2b). This unique elemental distribution may be related to the thermodynamically preferable formation of the Cr₇C₃ phase, which hinders the further incorporation of Cr atoms into lattices of the primary HEC phase via solid-solution reactions. X-ray diffraction (XRD) pattern and corresponding Rietveld refined results (Supplementary Fig. 3) as well as high-magnification high-angle annular dark field (HAADF)-STEM images (Supplementary Fig. 4) indicate that the core-shell intermediate

powders only consist of the face-centered cubic (*fcc*)-HEC phase and the orthorhombic Cr₇C₃ phase, without any other impurities. All these results together validate the successful synthesis of HEC/Cr₇C₃ core-shell intermediate powders.

We subsequently densified these HEC/Cr₇C₃ intermediate powders using the spark plasma sintering (SPS) technique. Figure 2a shows the morphology of densified samples after corrosion in aqua regia, revealing that a fully dense structure embedded with a contiguous network has been constructed. The high-magnification SEM image in Fig. 2b clearly indicates there are two distinct phases, with the bright phase uniformly surrounding the dark phase. The accumulation of Cr (see Fig. 2c) in the bright phase suggests that the contiguous network is made of Cr₇C₃, while the remaining majority is HEC with Ta, Ti, Zr, Hf, and Nb elements (Fig. 2d–h). To further investigate their structures and compositions, we conducted HAADF-STEM imaging. The line scanning results in Figs. 2i, j confirm that the distribution of Cr differs significantly from those of other elements, consistent with EDS mapping results (Supplementary Fig. 5). The high-magnification HAADF-STEM image (see Fig. 2k) reveals that the boundaries are distinct and clean at the atomic scale, without amorphous phases. Combined with the selected area electron diffraction (SAED) pattern in Fig. 2l, the upper grain is verified to be orthorhombic Cr₇C₃, indicating that no phase transformation occurs during the SPS process.

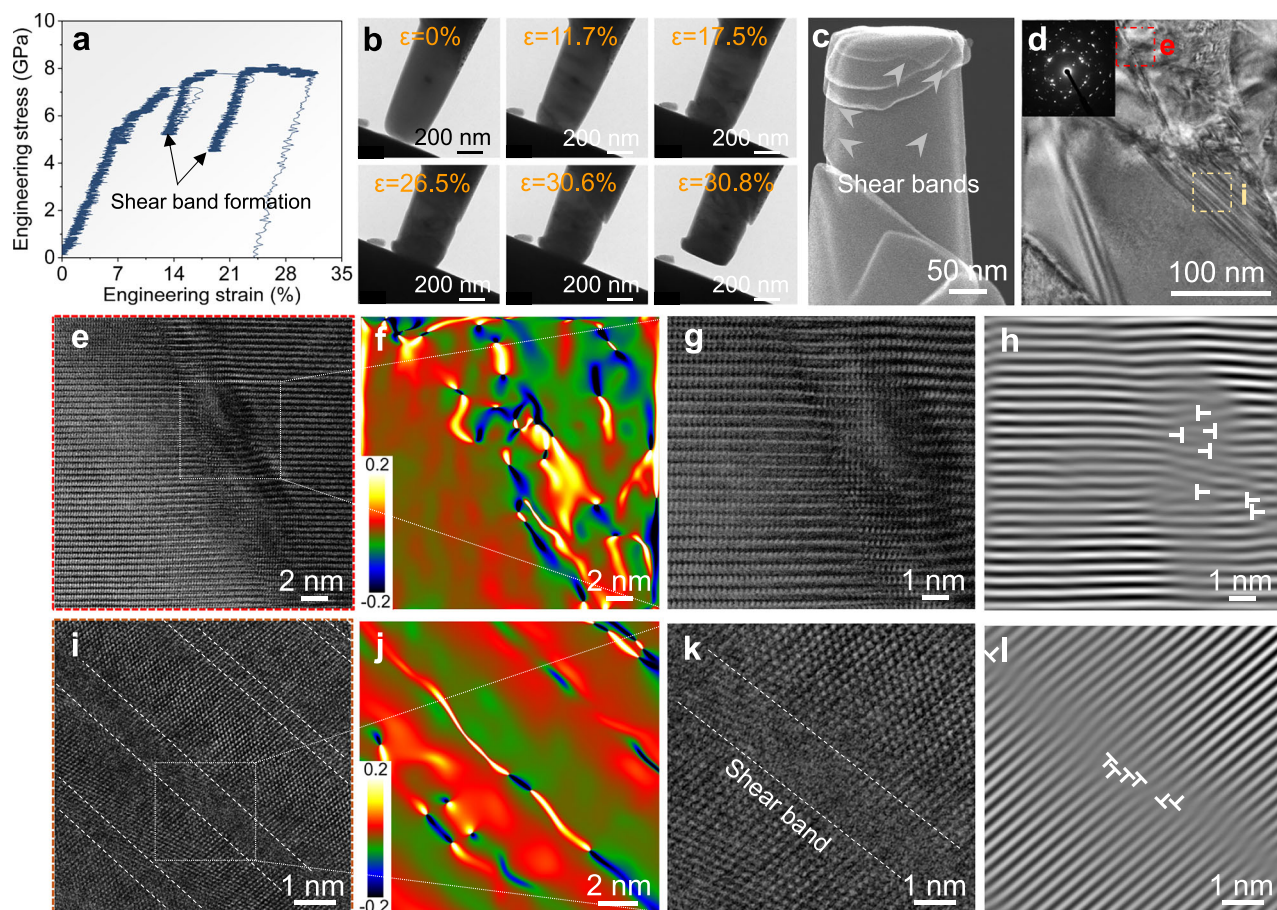


Fig. 3 | In-situ compression of Cr_7C_3 sub-micrometer-size pillars. **a** Typical compressive stress vs. strain curve. **b** Snapshots of a Cr_7C_3 pillar during compression in a transmission electron microscope (TEM), showing its ductility. **c** Low-magnification secondary electron (SE)-scanning transmission electron microscope (STEM) image of the pillar after compression, demonstrating the formation of shear bands in the pillar. **d** TEM image along with selected area electron diffraction

(SAED) pattern of the pillar after compression. **e, i** High-magnification bright field (BF)-STEM images of the highlighted areas in **(d)**. **f, j** Corresponding atomic elastic strain distribution maps of **(e, i)**, respectively. **g, k** Enlargements of the regions in **(e, i)**, respectively. **h, l** Inverse fast Fourier transform (IFFT) patterns of **(g, k)**, respectively. The white marks indicate dislocations. Source data are provided as a Source Data file.

Deformation behavior and mechanism of the Cr_7C_3 phase

To investigate the mechanical behavior of the Cr_7C_3 phase, we conducted in-situ mechanical testing of sub-micrometer-size pillars that were lifted out using the focused ion beam (FIB) technique at RT in a transmission electron microscope (TEM). Figure 3a displays the stress vs. strain profile of a representative Cr_7C_3 pillar. During compression, the flow stress of the pillar increases continuously before reaching a plateau of ~7.8 GPa, accompanied by the emergence of some serrations and significant drops in stress which may result from the formation of shear bands (this part will be discussed later). Notably, the pillar can experience an engineering strain of at least 30.8% without fracturing, proving good ductility of Cr_7C_3 that are even comparable to some intermetallic compounds such as Al_3Sm ²⁸. For comparison, we also tested sub-micron pillars of single-crystal HEC. The stress vs. strain curve in Supplementary Fig. 6a indicates that the HEC pillar experiences brittle fracture at a strain of 9.4%, reaching a stress of 13.3 GPa. The recorded compression process (Supplementary Fig. 6b and Supplementary Movie 1) confirms that the pillar has undergone sudden catastrophic fracture with no signs of plastic deformation, suggesting limited ductility of HEC. In terms of Cr_7C_3 , the snapshots in Fig. 3b (captured from Supplementary Movie 2) prove plastic deformation of the pillar during compression. Particularly, significant shear deformation is observed at 11.7% and 17.5% strains, correlating with the stress drops in Fig. 3a.

The secondary electron (SE)-STEM image of the post-compression pillar demonstrates the formation of shear bands within the pillar (Fig. 3c), providing compelling evidence for shear deformation occurring during the compression process. The polycrystalline SAED pattern in Fig. 3d signifies grain fragmentation in the upper section of the deformed pillar, without any visible cracks or voids. Additionally, the high-magnification bright field (BF)-STEM image (Fig. 3e) shows a newly formed boundary with distinct contrast. Further investigations on atomic elastic strain distribution suggest that the interface has undergone the most severe atomic strain (see Fig. 3f), implying the occurrence of dramatic plastic deformation. This conclusion can also be corroborated by the emergence of atomic-scale defects such as dislocations, as shown in the enlarged BF-STEM image (Fig. 3g) and corresponding inverse fast Fourier transform (IFFT) pattern (Fig. 3h). It is noteworthy that some ordered shear bands are present in the lower region of the pillar in Fig. 3d. The high-magnification BF-STEM image (Fig. 3i) and the corresponding atomic elastic strain distribution map (Fig. 3j) reveal considerable differences in crystallographic characteristics and atomic strain distributions between nanoscale shear bands and surrounding regions. Based on these observations, it is reasonable to speculate that the deformation does not localize within a specific shear band after its nucleation. Rather, the applied load seems to trigger the simultaneous formation of multiple shear bands, enabling the pillars to experience deformation without catastrophic failure. Figure 3k presents the enlarged view of Fig. 3i, which shows that the

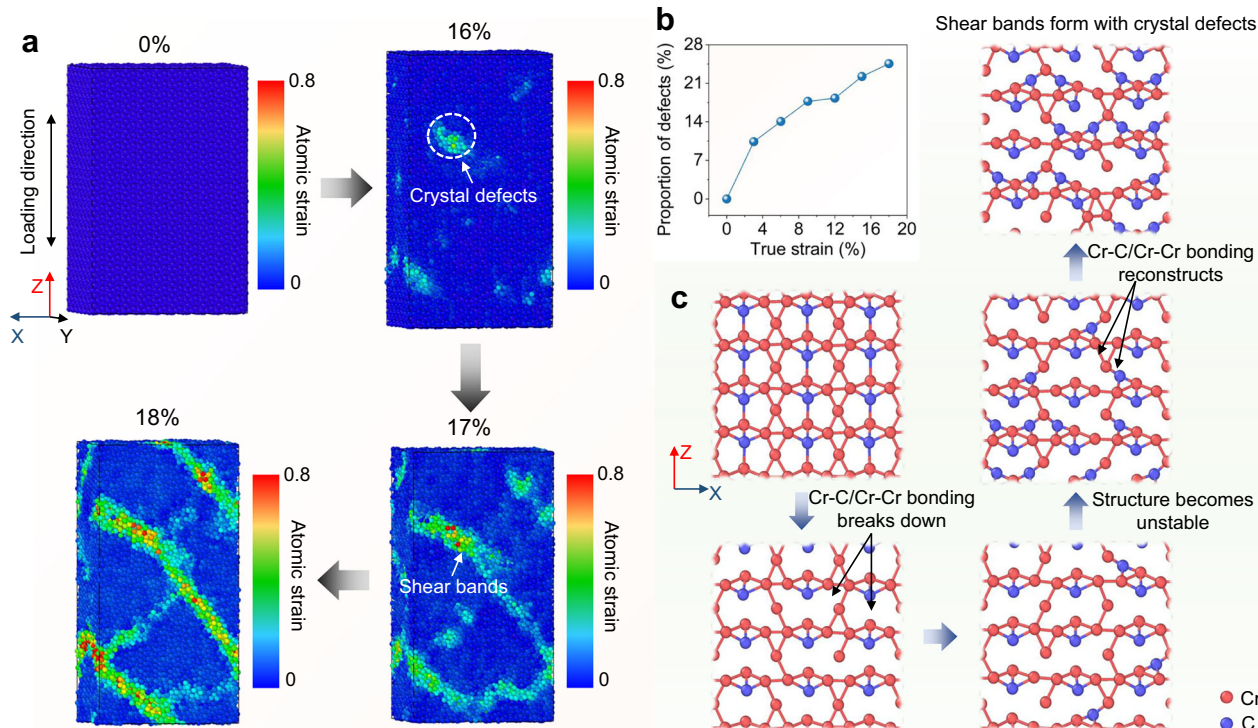


Fig. 4 | Simulation of the Cr_7C_3 phase during deformation. **a** Evolution of atomic strain in the Cr_7C_3 model under uniaxial tension along the [001] orientation. **b** Volume proportion change of crystal defects in the Cr_7C_3 model during

deformation. **c** Atomic evolution of shear-band regions during deformation. Cr and C atoms are colored in red and blue, respectively. Source data are provided as a Source Data file.

nanoscale shear bands with thicknesses of approximately 1–2 nm contain significant crystal defects, while the surrounding regions remain well-crystallized. The IFFT pattern in Fig. 3l confirms that atomic-scale defects are present exclusively within shear-band regions in Fig. 3k, supplying evidence to the confined crystallographic transformation in nanoscale shear bands. Shear bands with crystal defects can be also found in other regions of deformed pillars (see Supplementary Fig. 7). This plastic deformation mechanism considerably differs from the dislocation-dominated deformation mechanism typically observed in some metals²⁹, metalloids³⁰ and ceramics⁷, but is more akin to that in certain intermediate compounds such as Al_3Sm ²⁸, which exhibits similar shear band morphology and shear band-induced stress drops. Therefore, once the local stress reaches the limit of Cr_7C_3 , shear bands can form to relieve stress concentration, thereby accommodating plastic deformation and preventing catastrophic failure of Cr_7C_3 .

To gain further insight into the formation mechanism of shear bands in the Cr_7C_3 phase, we built a Cr_7C_3 model and simulate its deformation process using molecular dynamics (MD). It is important to note that, considering the periodic boundary condition and model size limitation, we here applied uniaxial tensile loading along the primary [001] direction to accurately simulate the plastic behavior of Cr_7C_3 , primarily because tensile loading is more effective in facilitating the formation of fractured surfaces within the size-limited models in comparison to compressive loading. Figure 4a shows the initial nucleation of clusters containing significant crystal defects at a tensile strain of 16%, and then these clusters gradually grow and connect to form shear bands as the tensile strain increases. To better quantify the crystal defects during deformation, the proportion of atoms that have deviated from their original positions was calculated. As shown in Fig. 4b, the curve representing the volume proportion of crystal defects as a function of true strain exhibits an approximately parabolic shape, reaching 24.5% at a 18% tensile strain. These findings verify the

occurrence of crystallographic transformation in shear bands. Additionally, to illustrate the atomic structural evolution in shear bands during loading, we chose the (010) plane as an example in Fig. 4c. Specifically, Cr-C and Cr-Cr bonds within six-membered rings are found to gradually break down, as the strain increases. The progressive breakdown of chemical bonds leads to the movement of partial atoms, followed by localized reconstruction of Cr-C and Cr-Cr bonds when some atoms come into close proximity. Such a gradual process facilitates the accommodation of plastic deformation in Cr_7C_3 , accompanied by the appearance of certain regions showing interior crystallographic symmetry i.e., crystal defects. This atomic evolution is distinct from that observed in brittle HEC, where the breakage of chemical bonds occurs almost simultaneously, ultimately resulting in a complete fractured surface (see Supplementary Fig. 8).

Mechanical properties of HEC/ Cr_7C_3 all-ceramics

Subsequently, we evaluated the fracture toughness K_{IC} and bending strength of the HEC/ Cr_7C_3 all-ceramics with different proportions of the Cr_7C_3 phase. The fracture toughness was measured using the single-edge notched beam (SENB) method, while the three-point bending test was employed to assess the bending strength of samples. The results in Fig. 5a demonstrate that K_{IC} values vary greatly with the proportion of Cr_7C_3 . For pure HECs, the K_{IC} is measured to be $3.1 \pm 0.9 \text{ MPa}\cdot\text{m}^{1/2}$, which is comparable to other HECs reported in the literature³¹. As the proportion of the Cr_7C_3 phase increases, K_{IC} values of HEC/ Cr_7C_3 all-ceramics rise dramatically. Notably, K_{IC} reaches the maximum of $12.5 \pm 1.5 \text{ MPa}\cdot\text{m}^{1/2}$ at a Cr_7C_3 proportion of ~25%, implying the crucial role of Cr_7C_3 in improving the fracture toughness of HECs. But as the proportion of the Cr_7C_3 phase continues to increase, the fracture toughness values begin to decline, primarily because the excessive Cr_7C_3 soft phase creates a continuous path for cracks. In addition, we used crack resistance curve (R-curve) analysis to further characterize the fracture toughness of HEC/ Cr_7C_3 all-ceramics.

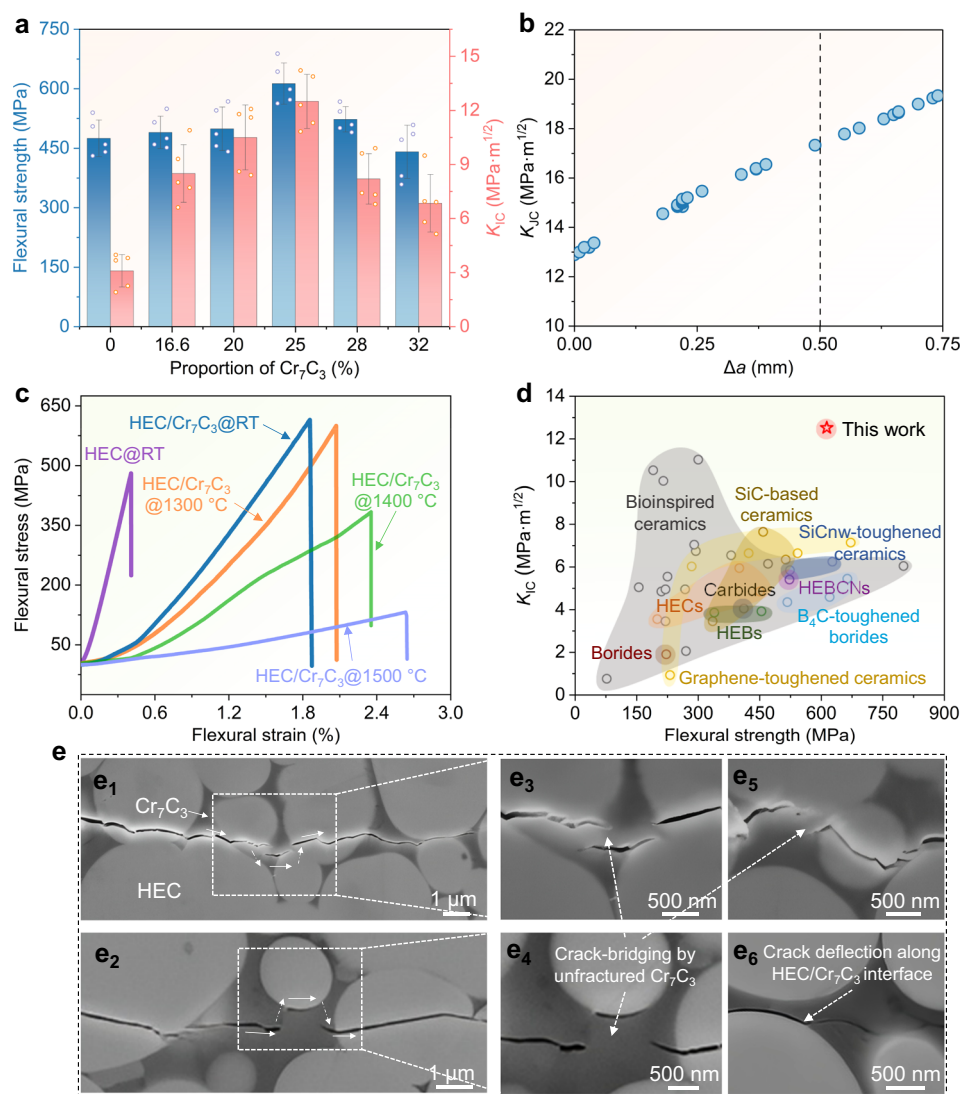


Fig. 5 | Mechanical properties and toughening mechanisms of high-entropy carbide (HEC)/Cr₇C₃ all-ceramics. a Fracture toughness K_{IC} and flexural strength of the samples with different proportions of Cr₇C₃. Error bars are generated with standard deviation. **b** Fracture toughness K_{IC} calculated from the J -integral and crack extension Δa according to the ASTM E1820-06 standard. **c** Flexural strength vs. strain of the representative pristine HEC and HEC/Cr₇C₃ samples tested at room temperature (RT), 1300 °C, 1400 °C, and 1500 °C. **d** Fracture toughness K_{IC} and flexural strength of HEC/Cr₇C₃ all-ceramics compared to those of other reported

structural ceramics^{10–15,32–53}. The colored shadings represent different categories of ceramic materials as labeled, and the circles indicate the specific values of these materials. **e** Crack propagation process: (e₁–e₂) Low-magnification scanning electron microscope (SEM) images, showing the overall propagation paths of cracks. The white arrows indicate the directions where the cracks propagate; (e₃–e₆) high-magnification SEM images, exhibiting the formation of unfractured plastic Cr₇C₃ ligaments bridging across cracks as well as crack deflection along HEC/Cr₇C₃ interfaces. Source data are provided as a Source Data file.

Figure 5b illustrates that their K_{IC} increases with crack extension (Δa), reaching ~17.3 MPa·m^{1/2} at a maximum valid Δa of 0.5 mm based on the ASTM criterion (raw force-displacement data can be found in Supplementary Fig. 9).

A similar trend is also observed in the bending strength of HEC/Cr₇C₃ all-ceramics. Specifically, the strength values increase from 475 ± 46 MPa to 613 ± 52 MPa with the gradual incorporation of the Cr₇C₃ phase from 0% to ~25% (see Fig. 5a). This increase in strength is mainly due to the enhanced densification of samples benefiting from the introduction of Cr₇C₃ soft phase. As excessive Cr₇C₃ of ~32% is incorporated, the strength of HEC/Cr₇C₃ samples decreases to 441 ± 67 MPa, primarily owing to the low inherent strength of soft Cr₇C₃. Although the bending strength values of pristine HECs and HEC/Cr₇C₃ all-ceramics are comparable, their stress-strain curves are distinct. Taking the pristine HEC and HEC/Cr₇C₃ (25% proportion of Cr₇C₃) samples as examples, as illustrated in Fig. 5c, the stress of HEC samples rises rapidly when the flexural strain increases, attaining the

maximum of 480 MPa at a strain of 0.4%. In comparison, the stress of representative HEC/Cr₇C₃ samples increases gradually, with a fracture strain exceeding 1.7%. These results prove that the deformation tolerance can be considerably improved by incorporating an appropriate amount of Cr₇C₃. The typical stress vs. strain profile of HEC/Cr₇C₃ all-ceramic samples shown in Supplementary Fig. 10a indicates that, while the samples exhibit a high ultimate compressive strength of 2.3 GPa, there are no significant signs of yielding during compression. This compressive behavior may be primarily due to the low content of Cr₇C₃ that is only sufficient to form a contiguous network. Additionally, the Vickers hardness of HEC/Cr₇C₃ all-ceramics has been measured to range from 25.4 ± 0.5 GPa to 20.4 ± 0.4 GPa, with applied loads varying from 0.1 kg to 1.0 kg (see Supplementary Fig. 10b).

In addition to RT, HEC/Cr₇C₃ all-ceramics are also promising for use at elevated temperatures. Specifically, the HEC/Cr₇C₃ samples exhibit a flexural strength of 594 ± 53 MPa at 1300 °C in an Ar

environment, indicating an excellent high-temperature strength retention of up to ~97% due to their good high-temperature stability. However, at a higher temperature of 1400 °C, there is a ~37% decrease in strength. As the temperature increases to 1500 °C, the strength values of HEC/Cr₇C₃ samples further drop to 131 ± 53 MPa. The mechanical deterioration is attributed to the high-temperature softening of the Cr₇C₃ plastic phase that has a relatively low melting point of ~1800 °C. This speculation is evidenced by the fractured surface morphology presented in Supplementary Fig. 11, which reveals that the samples tested at RT and 1300 °C tend to follow a transgranular fracture mode, while those tested at 1500 °C exhibit intergranular fracture due to the partial softening of Cr₇C₃. Moreover, it is worth mentioning that the in-situ bending strength testing was conducted over a short period. Under creeping conditions involving high stress and/or high temperature, the viscous deformation of Cr₇C₃ may occur over time.

We plot the fracture toughness and bending strength values of the developed bioinspired HEC/Cr₇C₃ all-ceramics and previously reported structural ceramics for a comparative study in Fig. 5d. The HEC/Cr₇C₃ all-ceramics not only exhibit relatively high bending strength but also demonstrate significantly greater fracture toughness than previously reported other structural ceramics, including bioinspired ceramics^{10–15,32–38}, graphene-toughened ceramics^{39–43}, SiC nanowire (SiCnw)-toughened ceramics^{41,42}, B₄C-toughened borides^{44,45}, individual borides⁴³ and carbides⁴⁶, SiC-based ceramics^{47,48}, high-entropy boron carbonitrides (HEBCNs)⁴⁹, HECs^{50–52}, and high-entropy borides (HEBs)⁵³, and are even comparable to ceramic matrix composites such as SiC fiber-reinforced Si₃N₄ composites (K_{IC} of 10.8 MPa·m^{1/2}, flexural strength of 357 MPa)⁵⁴, SiC nanofiber-reinforced SiC composites (K_{IC} of 5.1–10.5 MPa·m^{1/2}, flexural strength of approximately 320–380 MPa)⁵⁵, and SiC fiber-reinforced SiC composites (K_{IC} of 11.4–23.1 MPa·m^{1/2}, flexural strength of 216–420 MPa)⁵⁶. To illustrate the critical role of plastic Cr₇C₃ in improving fracture toughness, the crack propagation process is presented in Fig. 5e. Clearly, cracks propagate in zigzag paths, and several ways to suppressing crack propagation are identified. First, when a crack encounters a grain, it experiences extensive tearing and stretching. In this case, the ductility of Cr₇C₃ allows plastic deformation under load, leading to the formation of unfractured ligaments that bridge across cracks to hinder their opening and further propagation. Additionally, from an energy perspective, the Cr₇C₃ phase can function as a local crack arrester by alleviating the stress concentration at the crack tip through the generation of a sizable plastic deformation zone. This mechanism enables substantial energy dissipation that would otherwise promote the progression of cracks. Third, some cracks are observed to propagate along heterogeneous HEC/Cr₇C₃ interfaces, particularly at the end of the cracking process, which may be attributed to the low energy left at this final stage of cracking. In other words, when cracks reach Cr₇C₃/HEC interfaces, they do not possess enough energy to further penetrate into the HEC hard phase. Therefore, they tend to follow interfaces for a while before re-entering the Cr₇C₃ soft phase, where they are eventually annihilated. This process can give rise to crack deflection, extending the crack propagation paths that helps further improve the toughness of HEC/Cr₇C₃ all-ceramics.

In summary, to overcome the limitation of service temperatures below 1000 °C for bioinspired ceramics, we design bioinspired HEC/Cr₇C₃ all-ceramics that show great potential to serve up to 1300 °C. Specifically, these all-ceramic materials featuring a unique contiguous network distribution of the plastic Cr₇C₃ phase within the hard HEC phase, are developed through a high-entropy composition-engineering strategy. The developed HEC/Cr₇C₃ all-ceramics demonstrate excellent fracture toughness K_{IC} (12.5 ± 1.5 MPa·m^{1/2}) and flexural strength (613 ± 52 MPa), outperforming other structural materials reported previously. More importantly, they can retain ~97% of their flexural strength (594 ± 53 MPa) up to 1300 °C, exceeding what could be expected from other bioinspired ceramics. Further in-situ sub-

micron pillar compression tests and theoretical calculations confirm that the Cr₇C₃ phase can accommodate plastic deformation with an engineering strain of ~30.8% by forming multiple nanoscale shear bands, showing ductility that is even comparable to some intermetallic compounds. Such a unique plastic characteristic of Cr₇C₃ along with its contiguous network distribution results in multiple toughening mechanisms, including crack-bridging by unfractured Cr₇C₃ ligaments and crack deflection in the HEC/Cr₇C₃ all-ceramics. Our work successfully explores tough and strong bioinspired all-ceramics that can serve up to 1300 °C, providing a strategy to facilitate further design of bioinspired ceramics capable of operating at higher temperatures e.g., substituting Cr₇C₃ with other plastic high-temperature ceramic phases.

Methods

Sample synthesis

Commercially available powders, including HfO₂, Ta₂O₅, Nb₂O₅, Cr₂O₃ (purity: 99.9%, particle size: 1–3 μm, McLean Biochemical Technology Co., Ltd., Shanghai, China), TiO₂ (purity: 99.99%, particle size: 100–300 nm, McLean Biochemical Technology Co., Ltd., Shanghai, China), ZrO₂ (purity: 99.9%, particle size: 200 nm, McLean Biochemical Technology Co., Ltd., Shanghai, China), and carbon (purity: 99.95%, particle size: ≥100 mesh, Shanghai Aladdin Bio-Chem Technology Co., Ltd., Shanghai, China), were used as starting materials. The HEC/Cr₇C₃ core-shell intermediate powders were synthesized using a self-made ultrafast high-temperature synthesis (UHTS) apparatus. Specifically, the aforementioned metallic oxide and carbon powders were equimolarly weighed according to the ratio of the reaction equation, and then they were mixed with ethanol through ball milling for more than 24 h. After milling, the ethanol was evaporated using a rotatory evaporator. The resulting mixed powders were pressed into cylindrical green body samples with a diameter of 16 mm and a height of 2 mm. Subsequently, the pressed green body samples were placed between two pellets of graphite felt with a size of 130 mm × 10 mm × 6.5 mm (Av Carb Felt G650, Fuel Cell Store, Bryan, USA). An alternating current (AC, 100–250 A) was applied to both ends of the pellets, heating the samples to 1900 °C within 20 s under an argon atmosphere at atmospheric pressure. Note that the synthesis duration should not be too long; otherwise, the content of Cr₇C₃ would decrease. The surface temperature of the graphite felt was measured by an infrared thermometer (M313, SensorTherm, Lamspringe, Germany) during the synthesis process. After holding this temperature for 60 s, the samples were naturally cooled down to RT. The resulting samples were further sieved through a 200-mesh screen to obtain HEC/Cr₇C₃ core-shell intermediate powders. Afterward, the as-synthesized intermediate powders were densified using an SPS device (SPS-3.20MK-IV, SUMISEKI, Nagoya, Japan). These intermediate powders were placed in a graphite mold with an inner diameter of 35 mm and then were heated to 1600 °C with a heating rate of 100 °C/min, under a pressure of 30 MPa for a duration of 10 min. Following this, the samples were cooled with the furnace, and so the HEC/Cr₇C₃ all-ceramics were finally acquired. Overall, the final HEC/Cr₇C₃ all-ceramics are not insensitive to fabrication parameters, and therefore they can be scaled up.

Phase and structure characterization

The phase composition of samples was tested by XRD (X'pert PRO, PANalytical, Almelo, Netherlands), and the resultant patterns were further refined using a general structure analysis system software. The microstructure of samples was analyzed by a SEM (Supra-55, Zeiss, Oberkochen, Germany) equipped with EDS. The atomic structure of samples was characterized by an aberration-corrected STEM (HF5000, Hitachi High-Tech Co., Ltd., Tokyo, Japan) equipped with EDS operated at 200 kV.

In-situ compression of sub-micron pillars

Sub-micron pillars were lifted from HEC/Cr₇C₃ all-ceramic samples using FIB (Ga⁺ sources, 30 kV and low ion current of several to tens of

pA, FEI Helios NanoLab 600 dual-beam FIB system, FEI Co., Ltd., Oregon, USA). To minimize ion-beam irradiation damage, a final low energy ion-beam (5 kV, 1.5 pA) was used to clean the as-lifted pillar surface to reduce the thickness of damaged layer. In-situ mechanical testing at RT was conducted by using a Hysitron PicoIndenter (PI95, Hysitron Inc., Minneapolis, USA) inside a JEOL 2100 F TEM (JEOL Ltd. Tokyo, Japan). A Gatan 833 camera (Gatan Inc., Pleasanton, USA) was employed to record the in-situ movie inside JEOL 2100 F TEM. The mechanical loading was conducted under displacement control, with a constant loading rate of approximately $2 \text{ nm} \cdot \text{s}^{-1}$.

Flexural strength and fracture toughness characterization

The bending strength of samples was assessed by the three-point bending testing method according to ASTM D790-03³⁹. The testing samples were machined to dimensions of $3 \text{ mm} \times 4 \text{ mm} \times 35 \text{ mm}$, and the support span was set to 30 mm. Notably, the in-situ bending testing was conducted at elevated temperatures in an Ar environment. The bending strength and strain of the samples were calculated using the following formulas:

$$\sigma = 3PL/2bd^2 \quad (1)$$

$$\varepsilon = 6Dd/L^2 \quad (2)$$

where σ is bending strength, ε is the bending strain, P is the maximum load, L is the support span of the samples, b is the width of the samples, and d is the height of the samples. The fracture toughness of the samples was tested using the SENB method, according to ASTM E1820-06⁵⁷. The testing samples were machined to dimensions of $3 \text{ mm} \times 4 \text{ mm} \times 18 \text{ mm}$, and the support span was set to be 16 mm. The K_{IC} was calculated with the following equations:

$$K_{IC} = \frac{P_{IC}L}{BW^{3/2}} f\left(\frac{a}{W}\right) \quad (3)$$

$$f\left(\frac{a}{W}\right) = \frac{3\left(\frac{a}{W}\right)^{1/2} \left[1.99 - \left(\frac{a}{W}\right)\left(1 - \frac{a}{W}\right)\left(2.15 - \frac{3.93a}{W} + 2.7\left(\frac{a}{W}\right)^2\right)\right]}{2\left(1 + \frac{2a}{W}\right)\left(1 - \frac{a}{W}\right)^{3/2}} \quad (4)$$

where P_{IC} is the maximum load in the SENB tests, S is the support span, B is the thickness of the samples, W is the width of the samples, and a is the notch depth. The K_{IC} was measured from J -integral according to the ASTM E1820-06 criterion. The equations are as follows:

$$K_{IC} = \sqrt{JE} \quad (5)$$

$$J = J_{el} + J_{pl} \quad (6)$$

$$J_{el} = \frac{K_{IC}^2}{E'} \quad (7)$$

$$E' = E(1 - \nu^2) \quad (8)$$

where E is the Young's modulus and ν is the Poisson's ratio. The plastic contribution J_{pl} was calculated using the following formula:

$$J_{pl} = \frac{1.9A_{pl}}{Bb} \quad (9)$$

where A_{pi} is the plastic area under the load-displacement curve, B is the width of samples, and b is the uncracked ligament of samples. The crack extension Δa was calculated using the equivalence between

compliance and crack length in SENB tests. The compliance was computed from the relation $C = u/f$, where u and f are the displacement and force of each point after the initiation of a crack, respectively. The crack was recursively calculated using the following formulas:

$$\Delta a = a_n - a \quad (10)$$

$$a_n = a_{n-1} + \frac{W - a_{n-1}}{2} \frac{C_n - C_{n-1}}{C_n} \quad (11)$$

where a_n and C_n are the crack length and compliance calculated at the n and $n-1$ steps respectively, and W is the width of samples. The Vickers hardness of samples was measured using a Vickers indenter (HVS-30Z, SCTMC Co. Ltd., Shanghai, China) with the different applied loads (0.1 kg, 0.2 kg, 0.3 kg, 0.5 kg, and 1 kg).

MD simulation

In MD simulations, uniaxial tensile loading is preferable to evaluate the plastic properties, since it can effectively facilitate the formation of fractured surfaces within the size-limited models. For uniaxial compression simulations, structural relaxations for the plastic studies may be problematic due to the limitation of periodic boundary conditions and the model size, leading to behavior that contradicts experimental observations. Therefore, uniaxial tensile loading has been widely used to accurately predict the experimental plastic behaviors of bulk materials in MD simulations²⁸. For the neuroevolution potential (NEP) constructions and classical MD simulations, machine learning force field-based ab initio molecular dynamics (AIMD) calculations were employed to obtain different configurations. One hundred configurations based on $1 \times 1 \times 2$ Cr_7C_3 supercell were generated through the NPT ensemble using the Nosé-Hoover thermostat to run for 2 ps with a timestep of 1 fs at 300 K. Then, static calculations on these configurations were performed to collect training data for the NEP construction. Taking the computational efficiency into account, a lower energy convergence criterion of 0.004 eV was used for the electronic self-consistency cycle with an energy difference less than 2 meV/atom guaranteed. The detailed training hyperparameters of the model are listed in Supplementary Table 1. The training outcomes in Supplementary Fig. 12 demonstrate the high accuracy of the NEP. Specifically, the effectiveness of regularization shows increasing-then-decreasing trends of all regularization loss functions during training, confirming the well-trained NEP. Meanwhile, the root mean square errors (RMSEs) in energy, force, and virial (1.5 meV, 177 meV/atom⁻¹, and 27.3 meV/atom⁻¹, respectively) were as low as previously reported machine-learning potentials for alloys and ceramics^{56–61}, indicating a high accuracy for our trained Cr_7C_3 NEP. The large scale atomic/molecular massively parallel simulator (LAMMPS) package was utilized to perform MD simulations in conjunction with the NEP. A $10 \times 6 \times 24$ supercell of 57600 atoms was built based on the Cr_7C_3 conventional cell and equilibrated in the NPT ensemble at 300 K for 10 ps. The relaxed model was then performed to uniaxial tension along the (001) direction at a strain rate of $10^{10} \cdot \text{s}^{-1}$ at 300 K under the NPT ensemble. The Open Visualization Tool (OVITO) software was used to analyze the atomic strains and structure evolution of the Cr_7C_3 crystal structure during deformation⁶². The volume proportion of crystal defects was evaluated by calculating the atoms that have deviated from their original positions, i.e., forming interstitial atoms during deformation according to the following equation:

$$\text{Volume proportion of crystal defects} = n_{\text{inter}}/N \quad (12)$$

where n_{inter} is the number of interstitial atoms under different strains, and N is the number of total atoms in the Cr_7C_3 crystal structure.

Data availability

The data that supports the findings of this study are available in the article and supplementary materials file. Source data are provided with this paper. All the raw data relevant to the study are available from the corresponding author upon request. Source data are provided with this paper.

References

- Shackelford, J. F. Materials science for engineers. Upper Saddle River, New Jersey (2000).
- Ritchie, R. O. The conflicts between strength and toughness. *Nat. Mater.* **10**, 817–822 (2011).
- Ortiz, C. & Boyce, M. C. Bioinspired structural materials. *Science* **319**, 1053–1054 (2008).
- Peters, A. B. et al. Materials design for hypersonics. *Nat. Commun.* **15**, 3328 (2024).
- Waku, Y. et al. A ductile ceramic eutectic composite with high strength at 1,873 K. *Nature* **389**, 49–52 (1997).
- Hsu, S. M. & Shen, M. C. Ceramic wear maps. *Wear* **200**, 154–175 (1996).
- Zhang, J. et al. Plastic deformation in silicon nitride ceramics via bond switching at coherent interfaces. *Science* **378**, 371–376 (2022).
- Nepal, D. et al. Hierarchically structured bioinspired nanocomposites. *Nat. Mater.* **22**, 18–35 (2023).
- Wegst, U. G. K., Bai, H., Saiz, E., Tomsia, A. P. & Ritchie, R. O. Bioinspired structural materials. *Nat. Mater.* **14**, 23–36 (2015).
- Munch, E. et al. Tough, bio-inspired hybrid materials. *Science* **322**, 1516–1520 (2008).
- Magrini, T. et al. Transparent and tough bulk composites inspired by nacre. *Nat. commun.* **10**, 2794 (2019).
- Morits, M. et al. Toughness and fracture properties in nacre-mimetic clay/polymer nanocomposites. *Adv. Funct. Mater.* **27**, 1605378 (2017).
- Tan, G. et al. Nature-inspired nacre-like composites combining human tooth-matching elasticity and hardness with exceptional damage tolerance. *Adv. Mater.* **31**, 1904603 (2019).
- Guo, R., Hu, Z., Shaga, A. & Shen, P. Development of a nacre-like metal-ceramic composite with a brick-and-mortar structure and high ceramic content. *Compos. A Appl* **165**, 107347 (2023).
- Wilkerson, R. P. et al. A novel approach to developing biomimetic (“nacre-like”) metal-compliant-phase (nickel-alumina) ceramics through coextrusion. *Adv. Mater.* **28**, 10061–10067 (2016).
- Chaari, F., Halgrin, J., Markiewicz, É. & Drazetic, P. Spongy bone deformation mechanisms: experimental and numerical studies. *Eur. J. Comp. Mech.* **18**, 67–79 (2009).
- Dong, L. et al. Borrowed dislocations for ductility in ceramics. *Science* **385**, 422–427 (2024).
- Rost, C. M. et al. Entropy-stabilized oxides. *Nat. Commun.* **6**, 8485 (2015).
- Ye, B., Wen, T., Huang, K., Wang, C.-Z. & Chu, Y. First-principles study, fabrication, and characterization of ($\text{Hf}_{0.2}\text{Zr}_{0.2}\text{Ta}_{0.2}\text{Nb}_{0.2}\text{Ti}_{0.2}$)C high-entropy ceramic. *J. Am. Ceram. Soc.* **102**, 4344–4352 (2019).
- Meng, H., Wei, P., Tang, Z., Yu, H. & Chu, Y. Data-driven discovery of formation ability descriptors for high-entropy rare-earth monosilicates. *J. Materiomics* **10**, 738–747 (2024).
- Wen, Z. et al. Ultrastrong and high thermal insulating porous high-entropy ceramics up to 2000 °C. *Adv. Mater.* **36**, 2311870 (2024).
- Liu, Y., Yu, H., Meng, H. & Chu, Y. Atomic-level insights into the initial oxidation mechanism of high-entropy diborides by first-principles calculations. *J. Materiomics* **10**, 423–430 (2024).
- Zhuang, L. et al. Unveiling the oxidation mechanisms of high-entropy carbides through atomic-scale dynamic observation. *Adv. Mater.* **37**, 2417846 (2025).
- Tang, Z., Wen, Z., Zhuang, L., Yu, H. & Chu, Y. Enhanced oxidation resistance of high-entropy diborides by multi-component synergistic effects. *Sci. China Mater.* **67**, 3392–3400 (2024).
- Liu, Y. et al. Lattice distortion enhanced hardness in high-entropy borides. *Adv. Funct. Mater.* **35**, 2416992 (2025).
- Ye, B. et al. First-principles study, fabrication and characterization of ($\text{Zr}_{0.25}\text{Nb}_{0.25}\text{Ti}_{0.25}\text{V}_{0.25}$)C high-entropy ceramics. *Acta Mater* **170**, 15–23 (2019).
- Naughton-Duszová, A. et al. Dual-phase high-entropy carbide/boride ceramics with excellent tribological properties. *J. Eur. Ceram. Soc.* **44**, 5391–5400 (2024).
- Hu, X. et al. Amorphous shear bands in crystalline materials as drivers of plasticity. *Nat. Mater.* **22**, 1071–1077 (2023).
- Liu, B. Y. et al. Large plasticity in magnesium mediated by pyramidal dislocations. *Science* **365**, 73–75 (2019).
- Xu, W. et al. Uniting ultrahigh plasticity with near-theoretical strength in submicron-scale Si via surface healing. *Adv. Funct. Mater.* **34**, 2404694 (2024).
- Hu, J. et al. Superhard bulk high-entropy carbides with enhanced toughness via metastable in-situ particles. *Nat. Commun.* **14**, 5717 (2023).
- Dwivedi, G., Flynn, K., Resnick, M. & Gouldstone, S. SampathA. Bioinspired Hybrid Materials from Spray-Formed Ceramic Templates. *Adv. Mater.* **27**, 3073–3078 (2015).
- Gao, H. et al. Mass production of bulk artificial nacre with excellent mechanical properties. *Nat. Commun.* **8**, 287 (2017).
- Wat, A. et al. Bioinspired nacre-like alumina with a bulk-metallic glass-forming alloy as a compliant phase. *Nat. Commun.* **10**, 961 (2019).
- Wat, A. et al. Bioinspired nacre-like alumina with a metallic nickel compliant phase fabricated by spark-plasma sintering. *Small* **15**, 1900573 (2019).
- Behera, R. P. et al. Rational design and fabrication of hierarchical ceramics using bioinspired microstructures for tailorable strength and toughness. *Cell Rep. Phys. Sci.* **5**, 102140 (2024).
- Bouville, F. et al. Strong, tough and stiff bioinspired ceramics from brittle constituents. *Nat. Mater.* **13**, 508–514 (2014).
- Grossman, M. et al. Mineral nano-interconnectivity stiffens and toughens nacre-like composite materials. *Adv. Mater.* **29**, 1605039 (2017).
- Chen, K. et al. Graphene oxide bulk material reinforced by hetero-phase platelets with multiscale interface crosslinking. *Nat. Mater.* **21**, 1121–1129 (2022).
- Sun, C. et al. Embedding two-dimensional graphene array in ceramic matrix. *Sci. Adv.* **6**, eabb1338 (2020).
- Sun, J. et al. Toughening in low-dimensional nanomaterials high-entropy ceramic nanocomposite. *Compos. B Eng.* **231**, 109586 (2022).
- Li, Z., Guo, R., Li, L., Zheng, R. & Ma, C. Microstructure and fracture toughness of SiAlCN ceramics toughened by SiC_w or GNP. *Ceram. Int.* **49**, 29709–29718 (2023).
- An, Y. et al. Bioinspired high toughness graphene/ZrB₂ hybrid composites with hierarchical architectures spanning several length scales. *Carbon* **107**, 209–216 (2016).
- Rehman, S. S. et al. In situ synthesis and sintering of B₄C/ZrB₂ composites from B₄C and ZrH₂ mixtures by spark plasma sintering. *J. Eur. Ceram. Soc.* **35**, 1139–1145 (2015).
- Qiu, S. et al. B₄C-(Ti_{0.9}Cr_{0.1})B₂ composites with excellent specific hardness and enhanced toughness. *J. Am. Ceram. Soc.* **106**, 4013–4022 (2023).
- Liu, L., Vleugels, J., Huang, S., Wei, J. & Wang, Y. Strengthened interfacial bonding and its effects on fracture mode of TaC ceramics with addition of B. *J. Eur. Ceram. Soc.* **40**, 1067–1077 (2020).
- Li, Y., Wu, H., Kim, H.-N., Liu, X. & Huang, Z. Simultaneously enhanced toughness and strain tolerance of SiC-based ceramic

- composite by in-situ formation of VB_2 particles. *J. Eur. Ceram. Soc.* **37**, 399–405 (2017).
48. Xiang, L. et al. Fabrication and mechanical properties of laminated HfC-SiC/BN ceramics. *J. Eur. Ceram. Soc.* **34**, 3635–3640 (2014).
 49. Guan, J. et al. The new complex high-entropy metal boron carbide: Microstructure and mechanical properties. *J. Am. Ceram. Soc.* **105**, 6417–6426 (2022).
 50. Liu, D., Zhang, A., Jia, J., Zhang, J. & Meng, J. Reaction synthesis and characterization of a new class high entropy carbide (NbTaMoW). *C. Mater. Sci. Eng. A* **804**, 140520 (2021).
 51. Yu, D. et al. Pressureless sintering and properties of ($\text{Hf}_{0.2}\text{Zr}_{0.2}\text{Ta}_{0.2}\text{Nb}_{0.2}\text{Ti}_{0.2}\text{C}$) high-entropy ceramics: The effect of pyrolytic carbon. *J. Eur. Ceram. Soc.* **41**, 3823–3831 (2021).
 52. Liu, D., Zhang, A., Jia, J., Meng, J. & Su, B. Phase evolution and properties of (VNbTaMoW)C high entropy carbide prepared by reaction synthesis. *J. Eur. Ceram. Soc.* **40**, 2746–2751 (2020).
 53. Zhang, Z., Zhu, S., Liu, Y., Liu, L. & Ma, Z. Phase structure, mechanical properties and thermal properties of high-entropy diboride ($\text{Hf}_{0.25}\text{Zr}_{0.25}\text{Ta}_{0.25}\text{Sc}_{0.25}\text{B}_2$). *J. Eur. Ceram. Soc.* **42**, 5303–5313 (2022).
 54. Mo, R. et al. A high-temperature structural and wave-absorbing SiC fiber reinforced Si_3N_4 matrix composites. *Ceram. Int.* **47**, 8191–8199 (2021).
 55. Chen, H. et al. Microstructure and mechanical properties of multi-layer SiC nanofiber paper-reinforced SiC composites by the NITE method. *J. Am. Ceram. Soc.* **107**, 6410–6421 (2024).
 56. Yu, H. et al. Mechanical properties of 3D KD-I SiC_f/SiC composites with engineered fibre-matrix interfaces. *Compos. Sci. Technol.* **71**, 699–704 (2011).
 57. ASTM E1820-06. Annual Book of ASTM Standards, Vol 0301: *Metals-Mechanical Testing; Elevated and Low-Temperature Tests; Metallography*. ASTM International, (2006).
 58. Song, K. et al. General-purpose machine-learned potential for 16 elemental metals and their alloys. *Nat. Commun.* **15**, 10208 (2024).
 59. Li, Z., Graziosi, P. & Neophytou, N. Efficient first-principles electronic transport approach to complex band structure materials: the case of n-type Mg_3Sb_2 . *npj. Comput. Mater.* **10**, 8 (2024).
 60. Liu, Y. et al. Predicting mechanical and thermal properties of high-entropy ceramics via transferable machine-learning-potential-based molecular dynamics. *Adv. Funct. Mater.* **35**, 2418802 (2025).
 61. Meng, H., Liu, Y., Yu, H., Zhuang, L. & Chu, Y. Machine-learning-potential-driven prediction of high-entropy ceramics with ultra-high melting points. *Cell Rep. Phys. Sci.* **6**, 102449 (2025).
 62. we, A. Visualization and analysis of atomistic simulation data with OVITO-the Open Visualization Tool. *Modell. Simul. Mater. Sci. Eng.* **18**, 015012 (2010).

Acknowledgements

Authors acknowledge the financial support from the National Natural Science Foundation of China (52122204 to Y.C. and 52472072 to L.Z.), Guangzhou Basic and Applied Basic Research Foundation

(SL2024A04J01220 to Y.C.), Guangdong Basic and Applied Basic Research Foundation (2023B1515040011 to Y.C. and 2025A1515010644 to L.Z.), and Natural Science Basic Research Program of Shaanxi (2023-JC-YB-400 to Y.Q.)

Author contributions

Y.C. conceived and designed this work. Z.Z., Y.Q., and F.G. performed experiments. Y.L. and H.Y. performed calculations. Y.C. and L.Z. analyzed the data and wrote the manuscript. All authors commented on the manuscript.

Competing interests

The authors declare no competing interests.

Additional information

Supplementary information The online version contains supplementary material available at <https://doi.org/10.1038/s41467-025-59914-9>.

Correspondence and requests for materials should be addressed to Lei Zhuang or Yanhui Chu.

Peer review information *Nature Communications* thanks Paulo Branicio and the other, anonymous, reviewer(s) for their contribution to the peer review of this work. A peer review file is available.

Reprints and permissions information is available at <http://www.nature.com/reprints>

Publisher's note Springer Nature remains neutral with regard to jurisdictional claims in published maps and institutional affiliations.

Open Access This article is licensed under a Creative Commons Attribution-NonCommercial-NoDerivatives 4.0 International License, which permits any non-commercial use, sharing, distribution and reproduction in any medium or format, as long as you give appropriate credit to the original author(s) and the source, provide a link to the Creative Commons licence, and indicate if you modified the licensed material. You do not have permission under this licence to share adapted material derived from this article or parts of it. The images or other third party material in this article are included in the article's Creative Commons licence, unless indicated otherwise in a credit line to the material. If material is not included in the article's Creative Commons licence and your intended use is not permitted by statutory regulation or exceeds the permitted use, you will need to obtain permission directly from the copyright holder. To view a copy of this licence, visit <http://creativecommons.org/licenses/by-nc-nd/4.0/>.

© The Author(s) 2025